Robust Navigation of UAV using Inertial Sensors Aided by UWB and RTK GPS

Kristoffer Gryte*, Jakob M. Hansen†, Tor Arne Johansen‡, Thor I. Fossen‡

Center for Autonomous Marine Operations and Systems

Norwegian University of Science and Technology, Trondheim, 7491, Norway

Tight integration of ultra wideband (UWB) range measurements with real-time kinematic (RTK) aiding of inertial navigation for increased robustness to GNSS dropouts, is achieved using a double-differenced nonlinear observer. A stationary base station provides additional GNSS range measurements, upon which a double-differenced observer is formulated. The results are verified using a simulated unmanned aerial vehicle (UAV) with realistic inertial, GNSS and UWB measurements.

Nomenclature

A	Dynamics matrix
b	Angular velocity bias
C	Measurement matrix
e	Injection term
f	Specific force
K	Observer gain matrix
k	Constant tuning parameter
L	Scaling matrix
l	UWB Geometric distance
N	Integer ambiguity
P	Covariance matrix
p	Position
Q	Measurement covariance matrix
q	Unit quaternion attitude representation
R	State covariance matrix
U	Lyapunov function candidate
v	velocity
w	UWB white noise

Subscripts

i, h	Satellite number
j	UWB node number
k	Iteration number

Symbols

α	UWB rover clock bias
β	GNSS receiver clock bias
χ	Auxiliary state vector
δ	Perturbation term
δ	Transformed state vector 3
ϵ	GNSS range atmospheric noise
η	Transformed state vector
λ	Wavelength
μ	UWB range measurement
ν	Vector
ω	Angular velocity
ψ	Geometric distance from satellite to receiver
ρ	Pseudo-range measurement
$\hat{\sigma}$	Attitude observer injection term
φ	Carrier-phase measurement
ξ	Auxiliary state

Superscripts

b	Body frame
e	Earth-Centered-Earth-Fixed frame
n	North-East-Down frame
r	Rover (UAV) receiver
s	Base station receiver

*PhD Candidate, Department of Engineering Cybernetics, kristoffer.gryte@itk.ntnu.no, AIAA Student Member.
†PhD Candidate, Department of Engineering Cybernetics.
‡Professor, Department of Engineering Cybernetics.

I. Introduction

Within the last decade, the use of unmanned aerial vehicles (UAVs) have vastly increased due to lower cost and ease of use. The level of autonomy has increased as well, and UAVs are now able to complete complicated tasks autonomously. However, the landing phase of a UAV mission is often manually operated by a highly skilled UAV pilot. The primary reason for manual control is the fast adaptability and high precision required for safely landing a UAV in a small area. The high precision demand might not be satisfied by the on-board sensor-suite, which often has low accuracy in low-cost UAVs due to cost and weight constraints. Typical navigation avionics consists of a single-frequency global navigation satellite system (GNSS) receiver and a MEMS-based inertial measurement unit (IMU).

The measurements can be integrated to obtain higher precision than the stand-alone GNSS receiver precision. The integration is often achieved using a Kalman filter (KF) variant, which integrates the inertial measurements from acceleration to position, at high rate, while correcting the position estimate using the GNSS receiver data obtained at a lower rate. The attitude of the vehicle can also be estimated by the KF by using angular velocity or magnetometer measurements. In recent years nonlinear observers have been proposed to estimate position, linear velocity and attitude (PVA) of vehicles as an alternative to the widely used KF. The nonlinear observers have the advantage of proven (often global) stability conditions, smaller computational footprint and reduced need for linearization. In Ref. 1 and Ref. 2 a nonlinear complementary filter was proposed, which was expanded upon in Ref. 3 to an attitude and velocity observer dependent only on inertial, magnetometer and GNSS measurements. Furthermore, in Ref. 4 and Ref. 5, these results were expanded to include the quaternion representation of attitude in local and global coordinate frames. For an extensive overview of attitude estimators see Ref. 6.

One way to increase the precision of the PVA estimates is to utilize a tightly coupled integration scheme, integrating the inertial measurements with global range measurements from the satellites to the receiver, instead of using the global position estimates from the receiver. The GNSS measurements are thereby in the range domain instead of the position domain, allowing aiding by pseudo-range or carrier-phase measurements. Tightly coupled integration have traditionally been done using a KF variant; Ref. 7 and Ref. 8, with nonlinear observers recently being proposed; Ref. 9, Ref. 10, Ref. 11 and Ref. 12. Using carrier-phase measurements as aiding, introduces the integer ambiguities which are a constant range offset, given by a number of wavelengths. If the ambiguities can be resolved correctly the carrier-phase measurements will typically have centimeter accuracy.

The global range measurements are subjected to disturbances from the atmosphere due to signal path obstructions in the ionosphere and troposphere. These atmospheric disturbances can be somewhat predicted using local and solar weather forecasts. Another option is to augment the measurement configuration by including a base station at a known position. The base station supplies the vehicle (often called the 'rover') with range measurements obtained at the base station, to be subtracted from the rover measurements, thereby reducing common disturbances. If the rover is within 20 km,[7] the atmospheric disturbances can be canceled in the differenced range measurements. In a differential GNSS configuration the integration uses the differenced range measurements to aid the inertial navigation. When resolving the integer ambiguities in real time, the configuration can be considered a Real-Time-Kinematic (RTK) configuration. The quality of an RTK position estimate is often divided into three categories: a) 'single', indicating same precision as a single-receiver configuration, b) 'float', where the integer ambiguities are considered real valued numbers giving a precision on decimeter level, or c) 'fixed', when the ambiguities have been resolved to integer values often with a precision on centimeter level. Maintaining a 'fixed' RTK position estimate is desirable when the accuracy requirements are high, such as during a fixed-wing UAV net landing.[13]

A drawback of the RTK positioning is the sensitivity to agile maneuvers and obstructed GNSS signal path, which can lead to loss of fix quality. If the RTK positioning looses sight of a satellite in the constellation, the integer ambiguity have to be determined again when the satellite is reintroduced. In order to improve the resistance to precision deterioration when satellites are obstructed the sensor configuration can be augmented with use of further aiding sensors, e.g. cameras, air speed sensors, or ultra wideband transceivers. Ultra wideband (UWB) technology has typically been used for indoor navigation due to its short range. The setup consists of a UWB receiver measuring the distance to one (or several) UWB nodes acting as pseudo-satellites. The UWB cannot, in practice, substitute the GNSS measurements in outdoor environment due to the short range, however it can aid the inertial navigation in GNSS denied or challenged areas, e.g. the UWB nodes can be placed strategically around the landing area to aid during the final part of a UAV flight. UWB technology have been used in other outdoor applications such as in Ref. 14 where inter-vehicle positioning

was achieved using DGPS in combination with UWB, or in Ref. 15 where position and heading of smoke divers equipped with IMU and UWB was estimated. Other previous work include Ref. 16 where double-differenced GPS measurements are coupled with a single UWB range measurement in a tightly coupled manner, using an unscented Kalman filter and a two-frequency GPS receiver. Their goal is to accurately determine the relative position between two UAVs in formation flight, with increased robustness to GPS loss-of-fix. Further, Ref. 17 presents a summary of the theoretical foundation for, and challenges related to, UWB self-localization systems, such as the Cramer-Rao lower bound and clock synchronization issues. Another UWB application is suggested in Ref. 18, where UWB position estimates are used to emulate GNSS measurements.

This paper considers a tightly-coupled integration of IMU and double-differenced GNSS range measurements for RTK applications using a nonlinear observer structure aided with single-differenced UWB range measurements. The main contribution of this paper is the addition of UWB range measurements to the nonlinear observer, which offers increased robustness when operating in GNSS challenged or denied areas. This addition requires the stability proof to be revisited, as the state vector for the translational motion observer is augmented to include timing parameters for the UWB signals.

A. Notation and Preliminaries

A column vector $x \in \mathbb{R}^3$ given as $x := [x_1; x_2; x_3]$ with transpose $x^\intercal$ has Euclidean norm $\|x\|_2$, while the skew-symmetric matrix, denoted $S(\cdot)$, is given as:

$$S(x) = \begin{bmatrix} 0 & -x_3 & x_2 \\ x_3 & 0 & -x_1 \\ -x_2 & x_1 & 0 \end{bmatrix},$$

such that $S(x_1)x_2 = x_1 \times x_2$, where $\times$ denotes the vector product. The attitude can be represented by a unit quaternion $q := [s_q; r_q]$ with length $\|q\|_2 = 1$, consisting of a real part $s_q \in \mathbb{R}$ and a vector part $r_q \in \mathbb{R}^3$. The product between two quaternions, q and p, are given by the Hamiltonian product, denoted $q \otimes p$:

$$q \otimes p = \begin{bmatrix} s_q s_p - r_q^\intercal r_p \\ s_q r_p + s_p r_q + r_q \times r_p \end{bmatrix},$$

In the following 0 denotes a zero-matrix of appropriate dimensions.

In the following multiple coordinate frames will be used, where the frame will be indicated by the superscript unless otherwise stated. The Body-frame will be denoted b, while the global Earth-Centered-Earth-Fixed (ECEF) frame will be denoted e, and the local North-East-Down (NED) frame will be denoted n. A vector x might be decomposed in different coordinate frames, thus x^b and x^e refers to the same vector decomposed in the Body- and ECEF-frame. The rotation between frames are given by unit quaternions, e.g. $q_b^e = [s_{q_b^e}; r_{q_b^e}]$, with corresponding rotation matrix $R(q_b^e)x^b = x^e$ given as $R(q_b^e) := I + 2s_{q_b^e}S(r_{q_b^e}) + 2S(r_{q_b^e})^2$.

B. Paper Organization

The paper is organized as follows: in section II the configuration of sensors will be established, while section III states the problem formally. In section IV the proposed observer structure, consisting of a translational motion observer and a recent attitude estimator, will be introduced. Section V will show the obtained results using a state-of-the-art UAV simulator, with section VI summarizing the paper.

II. Problem Setup

This section describes the properties of UWB and RTK-GNSS, as well as why this type of sensors are beneficial to combine.

A. Real-Time-Kinematics GNSS

The idea behind RTK is to utilize differenced carrier-phase and pseudo-range measurements instead of measurements obtained at the rover, for computation of position. The differenced measurements are determined

by subtracting ranges obtained at a stationary base station from those obtained at a moving rover, thereby canceling some common error terms. The measurements, obtained from a constellation of m satellites, by the two receivers are pseudo-range, ρ, and carrier-phase, φ. Considering measurements from the ith satellite, the measurements are given as:

$$\rho_i^r = \psi_i^r + \beta^r + \epsilon_{\rho,i}^r, \tag{1}$$

$$\varphi_i^r = \psi_i^r + N_i^r \lambda + \beta^r + \epsilon_{\varphi,i}^r, \tag{2}$$

where $\psi_i^r = \|p_r^e - p_i^e\|_2$ is the geometric distance between the rover, r, and the satellite, i, at position p_i^e. The receiver clock range bias is denoted as $\beta^r := c\Delta_c$, where Δ_c is the clock bias and c is the speed of light. The receiver clock range bias is assumed to be slowly time-varying, and to be the same for all satellites in the constellation. The integer ambiguity is denoted N_i^r, with λ being the wavelength. The atmospheric disturbances of the range measurements are denoted $\epsilon_{\rho,i}^r$ and $\epsilon_{\varphi,i}^r$, and consists of the systematic environmental errors due to signal path obstruction in the ionosphere and troposphere.

Introducing the base station measurements, expressed by substituting the superscript r to s, the range measurements can be differenced to cancel the common environmental terms. When the rover and base station are sufficiently close to each other, i.e. the baseline between them is less than 20km, the environmental errors experienced by the two receivers are considered to be the same, i.e. $\epsilon_{\rho,i}^r = \epsilon_{\rho,i}^s = \epsilon_{\rho,i}$ and $\epsilon_{\varphi,i}^r = \epsilon_{\varphi,i}^s = \epsilon_{\varphi,i}$.[7] For the ith satellite, the environmental errors are canceled in the single-differenced measurements:

$$\Delta\rho_i = \Delta\psi_i + \Delta\beta, \tag{3a}$$

$$\Delta\varphi_i = \Delta\psi_i + \Delta N_i\lambda + \Delta\beta, \tag{3b}$$

where $\Delta\rho_i = \rho_i^r - \rho_i^s$, $\Delta\varphi_i = \varphi_i^r - \varphi_i^s$, $\Delta\beta = \beta^r - \beta^s$, $\Delta N_i = N_i^r - N_i^s$, and $\Delta\psi_i = \psi_i^r - \psi_i^s$ is the length of the geometric baseline between rover and base station. The integer ambiguity is a vector, $\Delta N_i \in \mathbb{R}^m$, comprised of the ambiguities of the available satellites; $\Delta N_i = [N_1; N_2; \ldots; N_m]$.

The clock error $\Delta\beta$ can be removed by double-differencing the measurement against a satellite h at the same epoch:

$$\nabla\Delta\rho_{ih} = \nabla\Delta\psi_{ih}, \tag{4a}$$

$$\nabla\Delta\varphi_{ih} = \nabla\Delta\psi_{ih} + \nabla\Delta N_{ih}\lambda, \tag{4b}$$

where $\nabla\Delta\rho_{ih} = \Delta\rho_h - \Delta\rho_i$, $\nabla\Delta\psi_{ih} = \Delta\psi_h - \Delta\psi_i$, $\nabla\Delta\phi_{ih} = \Delta\phi_h - \Delta\phi_i$ and $\nabla\Delta N_{ih} = \Delta N_h - \Delta N_i$. It is assumed that the raw measurements are time stamped simultaneously by the receivers, such that the corresponding measurements for the two satellites can be found at the two receivers. Double-differencing the raw measurements reduces the dimensions of the observer, since clock error estimates are no longer needed. In the context of RTK-GNSS it can be advantageous to reduce the noise by double-differencing, since the residual measurement error, according to Ref. 19, should be less than $1/4$ wavelength to solve the integer ambiguity.

B. Ultra Wideband (UWB)

Ultra wideband is a radio technology that transmits over a very wide range of frequencies, typically several GHz. It is characterized by moderate range (typically 200 m) due to power limitations. UWB transmitters can not only be used for communication, but also for range measurements with sample rates in tens of Hertz. The technology has increased in popularity since the United States Federal Communications Commission (FCC) allowed for unlicensed use of the 3.1-10.6 GHz spectrum in 2002.[20] In particular, impulse-radio UWB (IR-UWB), has become popular for centimeter-level accuracy ranging applications.

Advantages with UWB include robustness to interference, resistance to multipath, low energy consumption,[21] small footprint, as well as good time resolution allowing for centimeter level precision of range measurements.[20] Disadvantages include range limitations, as well as the need for additional equipment in the UAV.

UWB ranging can be either synchronous or asynchronous.[20] For synchronous ranging, the time-of-flight (ToF) between the nodes are measured by comparing the timestamp of the received message with the current time in the node. For this reason, the ranging precision depends on accurate synchronization of the clocks of each node. This can be mitigated using asynchronous two-way ToF ranging, where one node transmits

a message to a second node, which simply transmits the message back. Again the first node compares the timestamp with the current time. However, as mentioned by Ref. 17, the one-way communication required by the asynchronous approach offers more flexibility since the range accuracy and rate of communication is not affected by introducing additional rovers to the system.

One common way to model UWB range measurements, as given in e.g. Ref. 22, is to include a bias term and a zero-mean noise term:

$$\mu_j^r = l_j^r + \alpha^r + \alpha_j + w_j^r. \tag{5}$$

Here, $l_j^r = \|p_r^e - p_j^e\|$ is the geometric distance between the rover r and the UWB node j. The noise term, w_j^r, represents the zero-mean white noise. The bias associated with the rover, including clock bias, radio oscillation frequencies and variations in the speed of light,[20] is summarized in α^r, while the equivalent bias terms associated with UWB node j are summarized in α_j. The experimental study in Ref. 21 shows a distance-dependence in the bias and in the noise standard deviation, which both are fit to a linear function using the least squares recursion. In the following, the bias and standard deviation will be considered constant, as in Ref. 15. Furthermore, only line-of-sight (LOS) operation will be considered. See Ref. 15 and Ref. 22 for studies on LOS and non-line-of-sight (NLOS) range measurements. By using the pseudo-range measurements from UWB node j to the rover and base station, the clock-bias from the node is removed using single differencing:

$$\Delta\mu_j = \Delta l_j + \Delta\alpha, \tag{6}$$

where $\Delta l_j = l_j^r - l_j^s$, and $\Delta\alpha = \alpha^r - \alpha^s$.

C. Interconnection

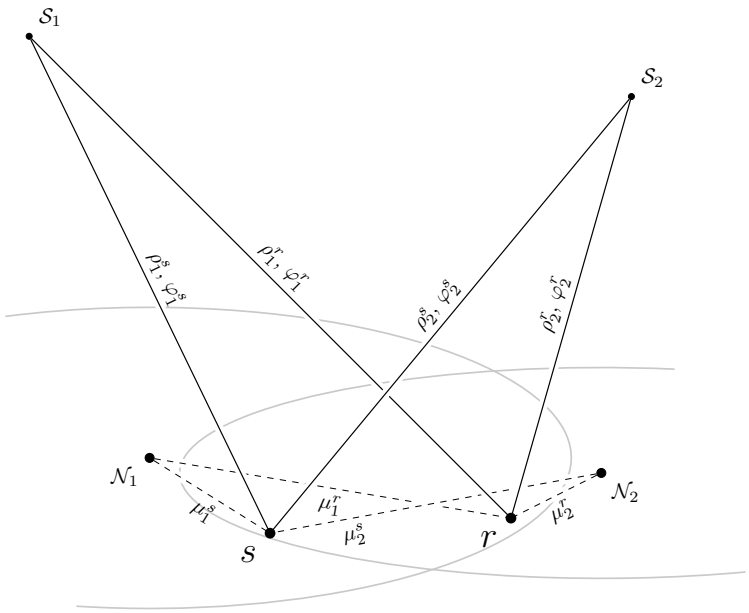

Figure 1: Conceptual setup of rover, base station, GNSS-satellites and UWB nodes

The reason for choosing to integrate UWB and RTK-GNSS is that they have some complimentary properties. While multipath can be a considerable error source in GNSS, this is not as pronounced for UWB due to the higher frequencies in the signal. On the other hand GNSS provides global coverage, whereas UWB coverage is significantly limited by the range of the signal. Additionally both systems are vulnerable to errors, if it is the only position sensor installed in the rover. Therefore the measurements from the two sensors can be beneficially fused, allowing for global coverage, and redundancy in critical situations such as landing a UAV, or UAV inspection in areas with high GNSS multipath noise levels.

A conceptual setup of the rover, base station, GNSS-satellites and UWB nodes is shown in figure 1. Two satellites, $\mathcal{S}_1$ and $\mathcal{S}_2$, are shown transmitting to the base station, s, and rover, r. Additionally, two UWB

nodes, $\mathcal{N}_1$ and $\mathcal{N}_2$, are depicted. The diagram has been simplified by including only two satellites and two UWB nodes. Both the rover and the base station are equipped with GNSS and UWB receiver, allowing for double-differencing of the GNSS and single-differencing UWB signals as explained in section II.A and section II.B. In addition, the rover is equipped with an inertial measurement unit (IMU) and a magnetometer. In order to solve the range measurement equations for the three dimensional position of the rover, the time, and the bias, at least five GNSS satellites must be within LOS. Similarly, the setup needs five UWB nodes that are located close to the base station, around an area of special interest, typically a region that is critical for the mission. The relative position of the nodes to the base station is assumed constant and known.

III. Problem Definition

Inertial navigation using a nonlinear observer in a dual receiver configuration is considered, where a stationary base station supplies a moving rover with GNSS range measurements. The common atmospheric disturbances can be canceled provided that the rover is sufficiently close to the base station, by determining the double-differenced range measurements. The inertial navigation is further aided by UWB measurements from a set of nodes. The nonlinear observer is an extension of the double-differenced observer developed in Ref. 10, extended to include single-differenced UWB range measurements.

This paper seeks to estimate the position, linear velocity and attitude (PVA) of a moving rover by use of tight integration of inertial measurements in the Body-frame aided by global GNSS and UWB range measurements. The GNSS data include pseudo-range and carrier-phase measurements, where the integer ambiguity are initially considered as real valued and can later be fixed to integer value for increase precision. The UWB system will provide short ranged measurements with high precision to be used when the rover enters an area of special interest, which might be GNSS denied or challenged. Estimation of the rover PVA is of interest as well as an evaluation of the benefits of using UWB measurements for additional aiding.

The kinematic model is stated as:

$$\dot{p}_r^e = v_r^e, \tag{7a}$$

$$\dot{v}_r^e = -2S\left(\omega_{ie}^e\right) v_r^e + f^e + g^e(p_r^e), \tag{7b}$$

$$\dot{q}_b^e = \frac{1}{2} q_b^e \otimes \begin{bmatrix} 0 \\ \omega_{ib}^b \end{bmatrix} - \frac{1}{2} \begin{bmatrix} 0 \\ \omega_{ie}^e \end{bmatrix} \otimes q_b^e, \tag{7c}$$

$$\dot{b}^b = 0, \tag{7d}$$

$$\dot{p}_s^e = 0. \tag{7e}$$

Here p_r^e and p_s^e are the position of the rover and base station, while q_b^e, v_r^e and ω_{ib}^b are the attitude represented by a unit quaternion, the linear and angular velocity of the rover, respectively. The angular velocity of the Earth, ω_{ie}^e, and the position dependent gravitational vector-function, g^e, are assumed known. The specific force experienced by the rover is denoted f^e, while b^b is the Body-frame gyro bias associated with the angular velocity measurements.

A. Measurement Assumptions

It is assumed that a sensor suite is mounted on the vehicle with inertial and global range measurement units. Moreover, it is assumed that the following measurements are available:

- Specific force as measured by an IMU, $f_{IMU}^b = f^b$.
- Angular velocity experiencing a bias, as measured by an IMU, $\omega_{ib,IMU}^b = \omega_{ib}^b + b^b$.
- Magnetic field as measured by a magnetometer, m^b.
- Pseudo-range as measured by a GNSS receiver from the ith satellite, ρ_i^r.
- Carrier-phase as measured by a GNSS receiver from the ith satellite, φ_i^r.
- UWB range as measured by a UWB receiver from the jth node, μ_j^r.

Furthermore, it is assumed that pseudo-range, carrier-phase and UWB measurements are available to the stationary base station, with at least $m \geq 5$ common satellites and $n \geq 4$ common UWB nodes.

IV. Nonlinear Observer

The proposed nonlinear observer structure consisting of a nonlinear attitude observer, a translational motion observer (TMO) and a gain computation, is visualized in figure 2. The block diagram also includes the required sensors; inertial, magnetometer, GNSS and UWB range sensors. Two GNSS receivers are necessary, one mounted on the rover and one on a stationary base station. The stationary receiver supplies the data for calculation of the satellite position, p_i^e, in addition to the range measurements. The UWB nodes are positioned such that the receiver on the rover can determine single-differenced range measurements.

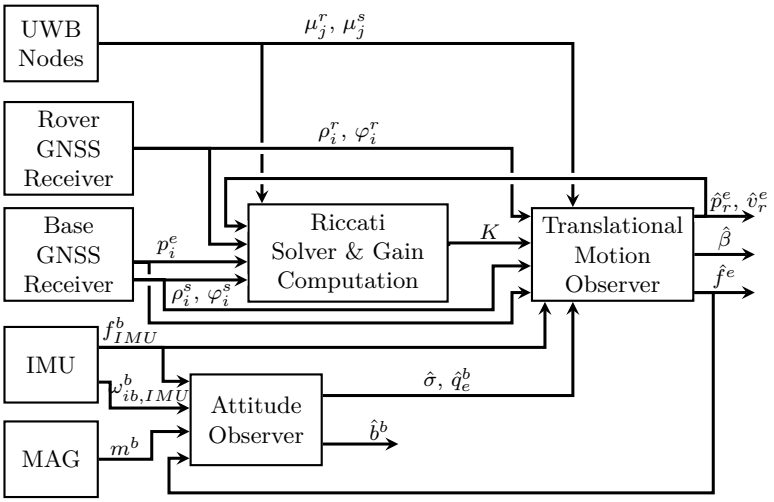

Figure 2: Block diagram of the proposed nonlinear observer structure

The proposed nonlinear observer is a modification to the loosely-coupled nonlinear observer initially presented in Ref. 5, which has been expanded in Ref. 9 to tightly-coupled systems using range and range-rate measurements, and further expanded in Ref. 10 where both a single-differenced and a double-differenced measurement structure was proposed.

The attitude observer is supplied with inertial measurements as well as a specific force estimate from the TMO. For the loosely-coupled system in Ref. 5 this was shown to be exponentially stable with a semiglobal region of attraction with respect to attitude observer initialization and local region of attraction with respect to translational motion observer initialization, due to the cascaded structure. An additional feedback, of rover position estimate, from the TMO to the gain computation is required to compute the injection terms necessary in the TMO.

The following sections will elaborate on the individual parts of the observer structure.

A. Attitude Observer

The attitude of the rover is determined as the rotation between Body- and ECEF-frame, using inertial measurements in Body-frame. The recent nonlinear attitude observer from Ref. 4, estimating the gyro bias in addition to the attitude as a unit quaternion, is restated as:

$$\dot{\hat{q}}_b^e = \frac{1}{2}\hat{q}_b^e \otimes \begin{bmatrix} 0 \\ \omega_{ib}^b - \hat{b}^b + \hat{\sigma} \end{bmatrix} - \frac{1}{2}\begin{bmatrix} 0 \\ \omega_{ie}^e \end{bmatrix} \otimes \hat{q}_b^e, \tag{8a}$$

$$\dot{\hat{b}}^b = \mathrm{Proj}\left(-k_I\hat{\sigma}, \|\hat{b}^b\| \leq M_{\hat{b}}\right). \tag{8b}$$

Here, the $\mathrm{Proj}(\cdot,\cdot)$-operator is a multi-dimensional saturation function that projects the gyro bias estimate to within a sphere with radius $M_{\hat{b}}$. The gain, k_I, is a positive constant, and $\hat{\sigma}$ is an injection term determined from two vectors in the Body-frame, ν_1^b and ν_2^b, with corresponding vectors in the ECEF-frame, ν_1^e and ν_2^e:

$$\hat{\sigma} = k_1\nu_1^b \times R(\hat{q}_b^e)^\intercal \nu_1^e + k_2\nu_2^b \times R(\hat{q}_b^e)^\intercal \nu_2^e, \tag{9}$$

where the tuning gains k_1 and k_2 satisfy $k_1 > k_p$ and $k_2 > k_p$ for some $k_p > 0$. The vectors in Body- and ECEF-frame can be chosen in various ways, and will here be considered as:

$$\nu_1^b = \frac{f_{IMU}^b}{\|f_{IMU}^b\|}, \quad \nu_1^b = \frac{\hat{f}^e}{\|\hat{f}^e\|}, \quad \nu_2^b = \frac{m^b}{\|m^b\|} \times \nu_1^b, \quad \nu_2^e = \frac{m^e}{\|m^e\|} \times \nu_1^e. \tag{10}$$

It is vital that the vectors ν_1^e and ν_2^e are not co-linear for the system to be observable. The magnetic field in ECEF-frame is assumed available, e.g. from a database. The estimated specific force, $\hat{f}^e$, is fed back from the translational motion observer.

B. Translational Motion Observer

Once the estimated attitude $\hat{q}_b^e$ and the injection term $\hat{\sigma}$ are established, they can be used in estimating the translational motion of the UAV. Additionally, the translational motion observer relies on the specific force measurement f_{IMU}^b, the GNSS pseudo-range measurements ρ_i^r and ρ_i^s from Eq. (1), the GNSS carrier-phase measurements φ_i^r and φ_i^s from Eq. (2), as well as the UWB pseudo-range measurements μ_j^r and μ_j^s from Eq. (5). Similarly to Ref. 23 the measurement noise is omitted in the analysis of nominal stability, but will be included in the simulations in section V.

By expanding the double-differenced observer from Ref. 10 with the UWB injection terms

$$\begin{aligned} e_{\mu,j} &= \Delta\mu_j - \Delta\hat{\mu}_j \\ &= \Delta\mu_j - \Delta\hat{l}_j^r - \Delta\hat{\alpha}_j^r, \end{aligned} \tag{11}$$

where $\Delta\hat{l}_j = \hat{l}_j^r - \hat{l}_j^s$, and $\Delta\hat{\alpha} = \hat{\alpha}^r - \hat{\alpha}^s$, the translational motion observer becomes:

$$\dot{\hat{p}}_r^e = \hat{v}_r^e + \sum_{i=1}^{m-1} \left(K_i^{p\rho} e_{\rho,mi} + K_i^{p\varphi} e_{\varphi,mi}\right) + \sum_{j=1}^{n} \left(K_j^{p\mu} e_{\mu,j}\right), \tag{12a}$$

$$\dot{\hat{v}}_r^e = -2S(\omega_{ie}^e)\hat{v}_r^e + \hat{f}^e + g^e(\hat{p}_r^e) + \sum_{i=1}^{m-1} \left(K_i^{v\rho} e_{\rho,mi} + K_i^{v\varphi} e_{\varphi,mi}\right) + \sum_{j=1}^{n} \left(K_j^{v\mu} e_{\mu,j}\right), \tag{12b}$$

$$\dot{\xi} = -R(\hat{q}_b^e)S(\hat{\sigma})f_{IMU}^b + \sum_{i=1}^{m-1} \left(K_i^{\xi\rho} e_{\rho,mi} + K_i^{\xi\varphi} e_{\varphi,mi}\right) + \sum_{j=1}^{n} \left(K_j^{\xi\mu} e_{\mu,j}\right), \tag{12c}$$

$$\hat{f}^e = R(\hat{q}_b^e)f_{IMU}^b + \xi, \tag{12d}$$

$$\dot{\hat{p}}_s^e = \sum_{i=1}^{m-1} \left(K_i^{s\rho} e_{\rho,mi} + K_i^{s\varphi} e_{\varphi,mi}\right) + \sum_{j=1}^{n} \left(K_j^{s\mu} e_{\mu,j}\right), \tag{12e}$$

$$\Delta\dot{\hat{\alpha}} = \sum_{i=1}^{m} \left(K_i^{\alpha\rho} e_{\rho,mi} + K_i^{\alpha\varphi} e_{\varphi,mi}\right) + \sum_{j=1}^{n} \left(K_j^{\alpha\mu} e_{\mu,j}\right), \tag{12f}$$

$$\nabla\Delta\dot{\hat{N}} = \sum_{i=1}^{m-1} \left(K_i^{Np} e_{\rho,mi} + K_i^{N\varphi} e_{\phi,mi}\right) + \sum_{j=1}^{n} \left(K_j^{N\mu} e_{\mu,j}\right). \tag{12g}$$

where K_*^{**} are gain matrices, and e_* are injection terms. The injection terms are defined as the difference between the true and the estimated measurements: $e_{\rho,mi} := \nabla\Delta\rho_{mi} - \nabla\Delta\hat{\rho}_{mi}$ and $e_{\varphi,mi} := \nabla\Delta\varphi_{mi} - \nabla\Delta\hat{\varphi}_{mi}$, in which the estimated double-differenced pseudo-range, carrier-phase and geometric range are given by

$$\begin{aligned} \nabla\Delta\hat{\rho}_{mj} &= \nabla\Delta\hat{\psi}_{mj} \\ \nabla\Delta\hat{\varphi}_{mj} &= \nabla\Delta\hat{\psi}_{mj} + \nabla\Delta\hat{N}_{mj}\lambda \\ \nabla\Delta\hat{\psi}_{mj} &= \|\hat{p}_r^e - p_j^e\|_2 - \|\hat{p}_r^e - p_m^e\|_2 - \|\hat{p}_s^e - p_j^e\|_2 + \|\hat{p}_s^e - p_m^e\|_2. \end{aligned}$$

To analyze the stability of the error state $\tilde{x} = x - \hat{x}$, with $\tilde{x} = \left[\tilde{p}_r, \tilde{v}_r, \tilde{f}, \tilde{p}_s, \Delta\tilde{\alpha}, \nabla\Delta\tilde{N}\right]^\intercal$, with $\nabla\Delta\tilde{N}_{mi} = \nabla\Delta N_{mi} - \nabla\Delta\hat{N}_{mi}$, it is desirable to put the system on the closed loop form $\dot{\tilde{x}} = (A - KC)\tilde{x}$. Thus, it is

necessary to express the injection terms by the error state $\tilde{x}$:

$$e_{\mu,j} = \|p_r^e - p_j^e\|_2 - \|p_s^e - p_j^e\|_2 - \|\hat{p}_r^e - p_j^e\|_2 + \|\hat{p}_s^e - p_j^e\|_2 + \Delta\tilde{\alpha}. \tag{13}$$

Further, following Ref. 10, the norm $h(p_r^e) = \|p_r^e - p_j^e\|_2$ is approximated by a second order Taylor approximation.

$$h(p_r^e) = \|\hat{p}_r^e - p_j^e\|_2 + c_j^{r\intercal}\tilde{p}_r^e + \text{h.o.t.}, \tag{14}$$

where $c_\dagger^* = \frac{\hat{p}_*^e - p_\dagger^e}{\|\hat{p}_*^e - p_\dagger^e\|_2}$, with $\dagger \in \{i,j\}$ and $* \in \{r,s\}$, is a general expression for the estimated line-of-sight vector between $*$ and $\dagger$. Through the same steps, a similar approximation can be found for the base station: $h(p_s^e) = \|\hat{p}_s^e - p_j^e\|_2 + c_j^s\tilde{p}_s^e + \text{h.o.t.}$. The coefficients are combined in $C_{\mu,j} = \left[c_j^r, 0, 0, -c_j^s, 0, 1, 0\right]$, $C_{\rho,mi} = [c_{mi}^r, 0, 0, -c_{mi}^s, 0, 0]$, $C_{\varphi,mi} = [c_{mi}^r, 0, 0, -c_{mi}^s, 0, \lambda 1_{i,m-1}]$, with $1_{i,m-1} = [0, \ldots, 1, \ldots, 0]$ describing an $(m-1)$-dimensional zero-vector with a non-zero ith element. The double-differenced coefficients are given as:[10]

$$c_{mi}^r = \frac{\hat{p}_r^e - p_i^e}{\|\hat{p}_r^e - p_i^e\|_2} - \frac{\hat{p}_r^e - p_m^e}{\|\hat{p}_r^e - p_m^e\|_2}, \quad c_{mi}^s = -\frac{\hat{p}_s^e - p_i^e}{\|\hat{p}_s^e - p_i^e\|_2} + \frac{\hat{p}_s^e - p_m^e}{\|\hat{p}_s^e - p_m^e\|_2}.$$

The injection terms can then be expressed as

$$\begin{aligned} e_{\mu,j} &= c_j^r\tilde{p}_r + c_j^s\tilde{p}_s + \Delta\tilde{\alpha} \ + \ \text{h.o.t.} \\ &= C_{\mu,j}\tilde{x} + \varepsilon_{l,j} + \varepsilon_{l_s,j}, \end{aligned} \tag{15}$$

$$e_{\rho,m,i} = C_{\rho,m,i}\tilde{x} + \varepsilon_{\psi,i} + \varepsilon_{\psi_s,i}, \tag{16}$$

$$e_{\varphi,m,i} = C_{\varphi,m,i}\tilde{x} + \varepsilon_{\psi,i} + \varepsilon_{\psi_s,i}, \tag{17}$$

where ε_* are the linearization errors from truncating the higher order terms in the Taylor expansion. By the same arguments that Ref. 9 applies for GNSS pseudo-range, the UWB linearization error is assumed. The linearization errors are bounded as:

$$\|\varepsilon_{l,j}\| \le \frac{1}{\underline{l}}\|\tilde{p}_r\|_2^2, \qquad \|\varepsilon_{l_s,j}\| \le \frac{1}{\underline{l}_s}\|\tilde{p}_r\|_2^2, \qquad \|\varepsilon_{\psi,i}\| \le \frac{1}{\underline{\psi}}\|\tilde{p}_r\|_2^2, \qquad \|\varepsilon_{\psi_s,i}\| \le \frac{1}{\underline{\psi}_s}\|\tilde{p}_r\|_2^2 \tag{18}$$

where $\underline{l}$ and $\underline{l}_s$ are positive, lower bounds on the distance between the UWB nodes and rover, and base station. Similarly $\underline{\psi}$ and $\underline{\psi}_s$ are positive, lower bounds on the geometric range between the satellites and rover, and base station.

Now the convergence of the estimates can be analyzed, by expressing the error dynamics as:

$$\dot{\tilde{x}} = (A - KC)\,\tilde{x} + \delta_1(t,\tilde{x}) + \delta_2(t,\tilde{\chi}) + \delta_3(t,\tilde{x}), \tag{19}$$

where $\tilde{\chi} = \left[\tilde{r}, \tilde{b}\right]^\intercal$. As no additional dynamics are introduced by the UWB measurements, this is similar to Ref. 10. All the terms have been augmented to accommodate the inclusion of the UWB bias term $\Delta\alpha$ to the state-space. Ref. 5 shows that $\delta_1(t,\tilde{x}) = [0; \delta_{12}(t,\tilde{x}); 0; 0; 0; 0]$, where $\delta_{12}(t,\tilde{x}) = -S(\omega_{ie}^e\tilde{x}_2 + (g^e(p_r^e) - g^e(p_r^e - \tilde{x}_1))$, and further that $\delta_2(t,\tilde{\chi}) = \left[0; 0; 0; \tilde{d}; 0; 0\right]$, with

$$\tilde{d} = (I - R(\tilde{q}_b^e)^\intercal)\,R(q_b^e)\left(S(\omega_{ib}^b)f^b + \dot{f}^b\right) - S(\omega_{ie}^e)\,(I - R(\tilde{q}_b^e)^\intercal)\,R(q_b^e)f^b - R(\tilde{q}_b^e)^\intercal R(q_b^e)S(\tilde{b})f^b. \tag{20}$$

The most significant changes are that the matrices K and C have been expanded to include the gains and linearized coefficients associated with the UWB injection terms, and that $\delta_3(t,\tilde{x}) = K\varepsilon(t,\tilde{x})$ includes the UWB linearization terms $\varepsilon_{\mu,j}$ from Eq. (15) in addition to the GNSS linearization terms $\varepsilon_{\rho,i}$ and $\varepsilon_{\varphi,i}$ from

Eq. (16) and Eq. (17). The matrices are:

$$A = \begin{bmatrix} 0 & I_3 & 0 & 0 & 0 & 0 \\ 0 & 0 & I_3 & 0 & 0 & 0 \\ 0 & 0 & 0 & 0 & 0 & 0 \\ 0 & 0 & 0 & 0 & 0 & 0 \\ 0 & 0 & 0 & 0 & 0 & 0 \\ 0 & 0 & 0 & 0 & 0 & 0 \end{bmatrix}, \quad K = \begin{bmatrix} K_1^{p\rho} & \cdots & K_{m-1}^{p\rho} & K_1^{p\varphi} & \cdots & K_{m-1}^{p\varphi} & K_1^{p\mu} & \cdots & K_n^{p\mu} \\ K_1^{v\rho} & \cdots & K_{m-1}^{v\rho} & K_1^{v\varphi} & \cdots & K_{m-1}^{v\varphi} & K_1^{v\mu} & \cdots & K_n^{v\mu} \\ K_1^{\zeta\rho} & \cdots & K_{m-1}^{\zeta\rho} & K_1^{\zeta\varphi} & \cdots & K_{m-1}^{\zeta\varphi} & K_1^{\zeta\mu} & \cdots & K_n^{\zeta\mu} \\ K_1^{s\rho} & \cdots & K_{m-1}^{s\rho} & K_1^{s\varphi} & \cdots & K_{m-1}^{s\varphi} & K_1^{s\mu} & \cdots & K_n^{s\mu} \\ K_1^{\alpha\rho} & \cdots & K_{m-1}^{\alpha\rho} & K_1^{\alpha\varphi} & \cdots & K_{m-1}^{\alpha\varphi} & K_1^{\alpha\mu} & \cdots & K_n^{\alpha\mu} \\ K_1^{N\rho} & \cdots & K_{m-1}^{N\rho} & K_1^{N\varphi} & \cdots & K_{m-1}^{N\varphi} & K_1^{N\mu} & \cdots & K_n^{N\mu} \end{bmatrix}, \tag{21a}$$

$$C = \begin{bmatrix} C_{\rho,m,1}; & \cdots & C_{\rho,m,m-1}; & C_{\varphi,m,1}; & \cdots & C_{\varphi,m,m-1}; & C_{\mu,1}; & \cdots & C_{\mu,n} \end{bmatrix}. \tag{21b}$$

Here, n is the number of UWB-nodes, while m is the number of available satellites, which both may change with every epoch.

Due to the inclusion of the UWB injection terms, the proof of Proposition 1 in Ref. 9 is insignificantly modified. Firstly, Eq. (19) is transformed by $\eta = L_\theta \tilde{x}$ to assign a desirable time-scale structure to the dynamics. Here, $L_\theta = \text{blockdiag}\left(I_3, \frac{1}{\theta} I_3, \frac{1}{\theta^2} I_3, \frac{1}{\theta^3} I_3, \frac{1}{\theta^4} 1, \frac{1}{\theta^5} I_n, \frac{1}{\theta^6} I_m\right)$ to include the additional states. By following Ref. 9, the derivative of the Lyapunov function candidate $U(\eta, t) = \frac{1}{\theta} \eta^T P^{-1} \eta$ becomes:

$$\dot{U} \leq -\gamma_1 \|\eta\|_2^2 + \frac{2}{\theta} \|\eta\|_2 \cdot \|C^\intercal R^{-1}\| \cdot \|E_\theta\| \cdot \left(2 \sum_{i=0}^{m-1} (\varepsilon_{\psi,i}^2 + \varepsilon_{\psi,i}^2) + \sum_{j=0}^{n} (\varepsilon_{l,j}^2 + \varepsilon_{l_s,j}^2) \right) + \frac{1}{\theta} \gamma_2 \gamma_4 \|\eta\|_2^2 + \frac{1}{\theta^3} \gamma_3 \gamma_4 \|\eta\|_2 \cdot \|\tilde{\chi}\|_2,$$

where $E_\theta = C L_\theta C^+$, and where C^+ is the Moore-Penrose right pseudo-inverse of C. The constants γ_1, γ_2, γ_3 and γ_4 are positive constants, independent of θ. The rest of the proof follows Ref. 9, yielding exponentially stable error dynamics with a local region of attraction with respect to the initialization point. Here it is assumed that the UWB and GNSS ranges are upper and lower bounded, that their range measurements come from at least five satellites, where at least three of the LOS vectors are linearly independent, and that the position of their transponders are known. Further it is assumed that the specific force and its derivative are bounded, that $(A, R^{-\frac{1}{2}} C)$ is completely uniformly observable, that the initial conditions are nice, and that the observer gains are chosen appropriately, see Assumptions 1 and $3-8$ in Ref. 9 for details.

C. Riccati Solver

The few gains in the attitude observer are directly tuned, however, for the translational motion observer the gains must be time-varying and the large number of gains require other methods.

One approach to determine the gains is the Riccati solver, also utilized by the KF, where the discrete-time time-varying Riccati equation is solved giving the gain and the covariance matrices, K and P. The gain matrix is determined using the symmetric, positive definite matrices Q and R, which can be interpreted as the covariance of the process and measurement noise. The matrices P, Q and R can be stated similarly to when used in a KF, as the observer error dynamics is the same as for the KF thereby allowing the observer gain to stabilize and tune the error dynamics. The matrices are determined using an iterative process for each discrete time instance, k:

$$P_{k|k-1} = A_d P_{k-1|k-1} A_d^\intercal + Q^\intercal, \tag{22a}$$

$$K_k = P_{k|k-1} C^\intercal \left(C P_{k|k-1} C^\intercal + R \right)^{-1}, \tag{22b}$$

$$P_{k|k} = (I - K_k C) P_{k|k-1} (I - K_k C)^\intercal + K_k R K_k^\intercal. \tag{22c}$$

Here, $A_d = e^{A \Delta t_{IMU}}$ is the discretized A matrix, where Δt_{IMU} is the IMU sample rate. The Riccati solver can be implemented such that the covariance for the state estimate, $P_{k|k-1}$, $P_{k|k}$ and the gain matrix K_k are only updated when new range measurements arrive.

For the stability proof it is assumed that the gain matrix is found from the transformed error dynamics, Ref. 9:

$$K := \theta L_\theta^{-1} K_0 E_\theta, \tag{23}$$

where $\theta \geq 1$ is a tunings parameter, while $K_0 := PC^\intercal R^{-1}$ where P satisfies the time-scaled Riccati equation.

An accurate initialization method was proposed in Ref. 9, ensuring stability when the gain matrix K is determined by solving the time-varying Riccati equation.

V. Simulations

This section offers a simulation study of a UAV operating in GNSS denied or challenged areas. The goal of the simulations is to evaluate the UWB as aiding sensor and determine the effect it contributes to the state estimation.

A. Implementation

To simulate sensor data from a UAV, the simulator developed in Ref. 24 is used with an Aerosonde UAV model. The measurements are generated from eqs. (1), (2) and (5), at 5 Hz for the GNSS and 10 Hz for the UWB. Here, ψ_i^r and l_j^r are calculated from the known satellite and UWB node positions, with λ set to 0.1903 m. Measurement noise is added to the range measurements, where the GNSS noise are first order Markov processes and the UWB noise is white noise. The Markov processes have a time constant of 60s, and is generated from white noise with standard deviation of 5 m. Additional white noise is added to the GNSS measurements to simulate receiver noise with standard deviations of 0.10 m and 0.001 m for the pseudo-range and carrier-phase measurements, respectively. The white noise on the UWB measurements are simulated with standard deviation of 0.026 m corresponding to the BeSpoon UM100 UWB module, whereas the IMU data is simulated with noise levels corresponding to the Analog Devices 16488 IMU; acceleration: 0.0015m/s^2, angular rate: $0.16^\circ/\text{s}$ and magnetometer: 0.45mGauss.

The nonlinear observer is implemented in a corrector-predictor architecture [25, p. 300], where the corrector part consists of the aiding measurements and can be implemented at low rate, while the predictor part is implemented at IMU frequency. The observer runs at 400 Hz, which is the frequency of the IMU, while GNSS and UWB measurements arrive at their appropriate frequencies. When GNSS/UWB measurements are not received, the corresponding elements in the measurement matrix C, in the gain matrix K, and in the injection terms e are masked out.

For the attitude observer the parameters are chosen as $M_b = 0.0087, k_1 = 0.8, k_2 = 0.2, k_I = 0.004$. The gains in the translational motion observer are calculated using the discrete time-varying Riccati equation Eq. (22). The covariance matrices can be initialized as diagonal matrices, where the diagonal elements correspond to the individual state or measurement variance: In this simulation, the covariance matrices are given by $R = \text{blkdiag}(0.2I_{m-1}, 2 \cdot 10^{-6} I_{m-1}, 0.956 \cdot 10^{-4} I_n)$ and $Q = \text{blkdiag}(10^{-18} I_3, 10^{-5} I_3, 2.5 \cdot 10^{-8} I_3, 10^{-18} I_3, 10 I_n, 10^{-7} I_{m-1})$.

B. GNSS Dropout during Flight

During an outage in GNSS coverage the inertial navigation estimates will drift from the true value. It is therefore of interest to see how the addition of UWB measurements might prevent the estimates from drifting in GNSS challenged areas. This scenario compares the position estimates with and without UWB measurements for a simulated fixed-wing UAV in a steady, banked clockwise turn. A simulated dropout of GNSS measurements is enforced in the time interval from $35s$ to $60s$, as indicated by the solid vertical lines in figs. 3 to 6. Similarily the UAV is within range of the UWB nodes in the approximate interval of 30 to $62s$, as indicated by the dashed vertical lines in the same figures.

In this simulation, five UWB node are placed in the vicinity of the flight path. Four of the nodes form a square of height 10 m and width 600 m, placed vertically and perpendicular to the flight path. The fifth node is placed perpendicular to the centre of the square, in center height 500 m behind the square. The range of the UWB nodes is set to 700 m.

Two simulations are included: a) using only GNSS as aiding, and b) using GNSS and UWB as aiding. The results of the simulations are shown in figure 3 and figure 4, depicting the position estimation error in NED-frame. The estimation error of the base station is shown in dashed lines, with the rover estimation errors shown in solid lines. The period of GNSS dropout is shown between the two vertical solid lines, whereas the period in which the UWB measurements are available is shown with vertical dashed lines.

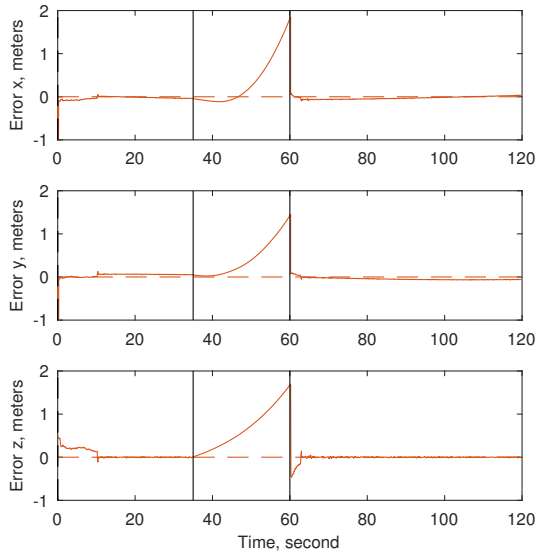

Figure 3: Position error using only GNSS aiding, GNSS dropout from 35s to 60s

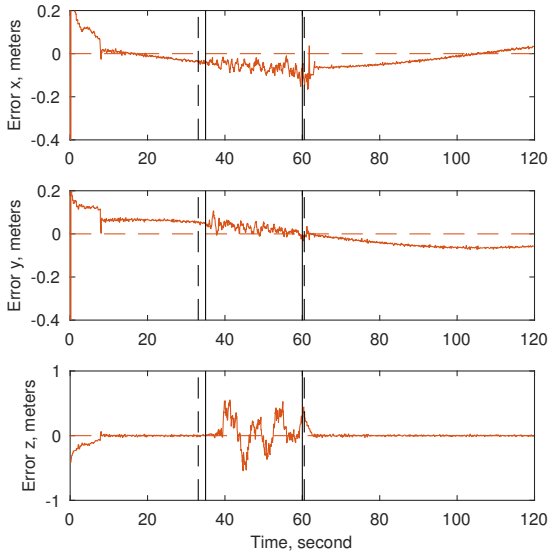

Figure 4: Position error using GNSS and UWB aiding, GNSS dropout from 35s to 60s

The estimation error in figure 3 is seen to divert due to the missing aiding, whereas the additional use of UWB nodes in figure 4 ensures a smaller diversion from the desired position (note the difference in scale on the vertical axes). For the case with UWB available the error of the rover position is less than 0.53 m away from the true position, whereas the case with only GNSS aiding experience rover position errors exceeding 2.91 m. In both cases, the position error is quickly reduced once the GNSS measurements are available again.

The errors in attitude estimation are shown in figure 5 and figure 6, and is expressed in Euler angles in the Body-frame. The qualitative behavior of the attitude error is not visibly affected by the GNSS dropout, neither with nor without UWB aiding.

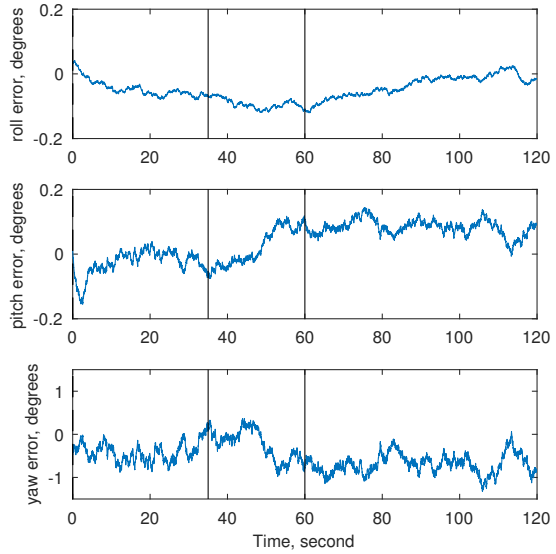

Figure 5: Attitude error using only GNSS aiding, GNSS dropout from 35s to 60s

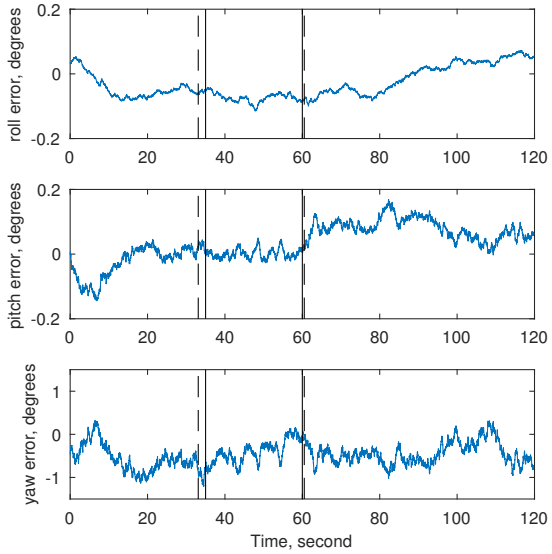

Figure 6: Attitude error using only GNSS and UWB aiding, GNSS dropout from 35s to 60s

C. Landing of UAV in GNSS Challenged Area

In order to test the performance of the proposed observer in GNSS challenged area, a landing scenario is investigated. The UAV starts with a relative altitude of 4 m to the desired landing zone. For this scenario the four first nodes form a square of size 5×5 m, which represent the corners of a net for the UAV to land in. This square is placed vertically and perpendicular to the flight path such that the landing target position of the UAV is in the center of the square. The fifth node is placed perpendicular to the centre of the square, 15 m behind it. The GNSS measurements are simulated with multipath errors when the UAV approaches landing. The multipath is simulated as additional Markov noise, which is generated from white noise with standard deviation of 1 m and 0.1 m for the pseudo-range and carrier-phase respectively. The Markov process has a time constant of 60s. Due to the increased GNSS noise, the R-elements corresponding to the GNSS carrier-phase and pseudo-range measurement were multiplied by a factor of 50, while all other tuning parameters remained the same.

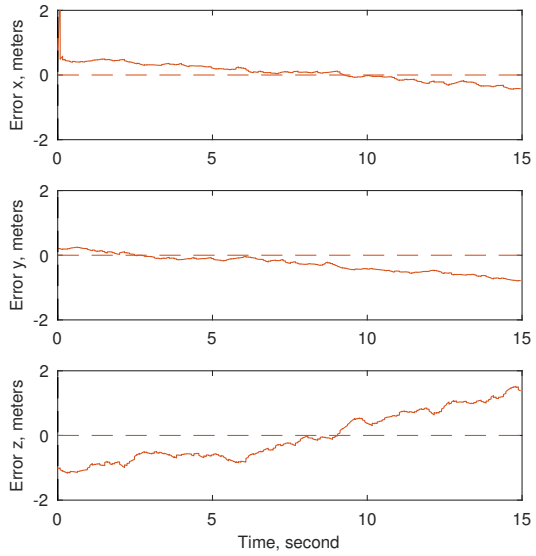

Figure 7: Position error using only GNSS aiding, simulated GNSS multipath

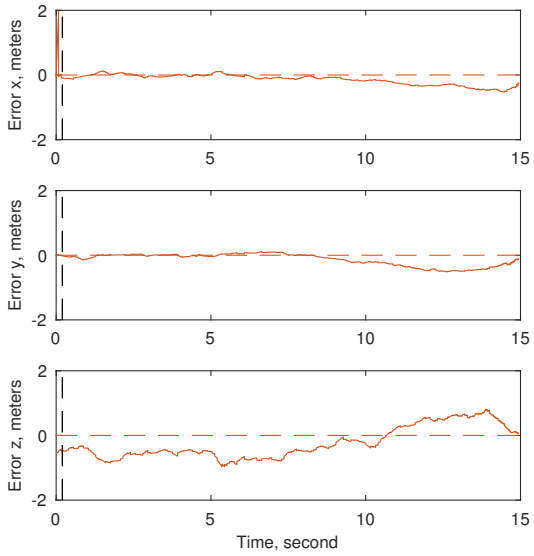

Figure 8: Position error using GNSS and UWB aiding, simulated GNSS multipath

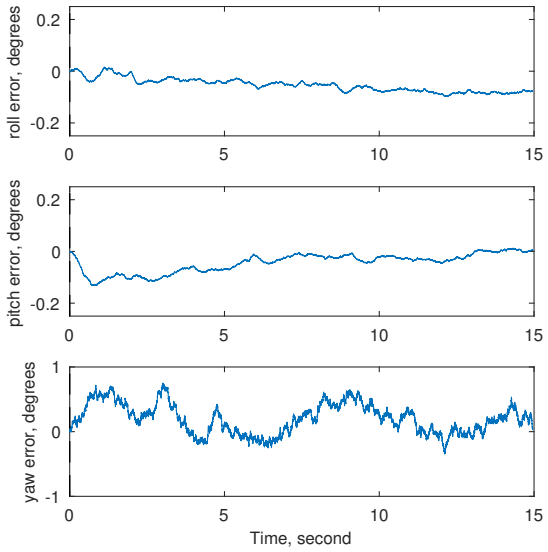

Figure 9: Attitude error using only GNSS aiding, simulated GNSS multipath

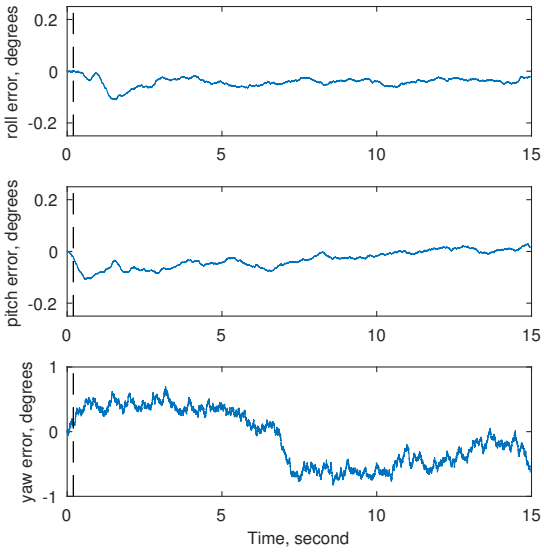

Figure 10: Attitude error using GNSS and UWB aiding, simulated GNSS multipath

The error in the estimated position without UWB aiding, shown in figure 7, generally has a larger magnitude than for the UWB aided case in figure 8. This is especially true for the final stage of the landing approach where the error in the estimated position is 0.32 m for the final position in the UWB aided case, whereas in the non-UWB case the norm is 1.60 m. A viable explanation for the improvements for the UWB aided case is the improved geometry configuration as the UAV gets closer to the landing target, since the angle between the UWB range measurements increase with decreasing distance to the net. The attitude errors for the two cases are of similar magnitude.

D. Monte Carlo Simulation

To compare the results with and without UWB, 100 simulations of the landing scenario in section V.C are run. For each set of simulated measurements, the observer is run once with and once without UWB measurements. Figure 11 shows a comparison of the root mean square error (RMSE) of the end position for the two cases, while Table 1 shows the RMSE averaged over the 100 simulations. The inclusion of UWB measurements decreases the rover position RMSE of the end point by close to three orders of magnitude: the norm of the RMSE averaged over all the simulations is reduced from 1.37 m to 0.584 m. The reduction is particularly pronounced in the z-axis. However, the inclusion of UWB increases the norm of the RMSE for the final base station position from $2.40 \cdot 10^{-9}$ m to $1.75 \cdot 10^{-5}$ m^2, but they are both zero for practical considerations.

Table 1: End position mean square errors (RMSE), landing scenario

	Rover Position (m)		
	x	y	z
GNSS	$4.31 \cdot 10^{-1}$	$5.34 \cdot 10^{-1}$	1.05
GNSS+UWB	$3.70 \cdot 10^{-1}$	$2.43 \cdot 10^{-1}$	$2.50 \cdot 10^{-1}$

Table 2: Position root mean square errors (RMSE), circle scenario.

	Rover Position(m)		
	x	y	z
GNSS	$5.03 \cdot 10^{-2}$	$4.67 \cdot 10^{-2}$	$9.31 \cdot 10^{-3}$
GNSS+UWB	$5.02 \cdot 10^{-2}$	$4.66 \cdot 10^{-2}$	$9.05 \cdot 10^{-3}$

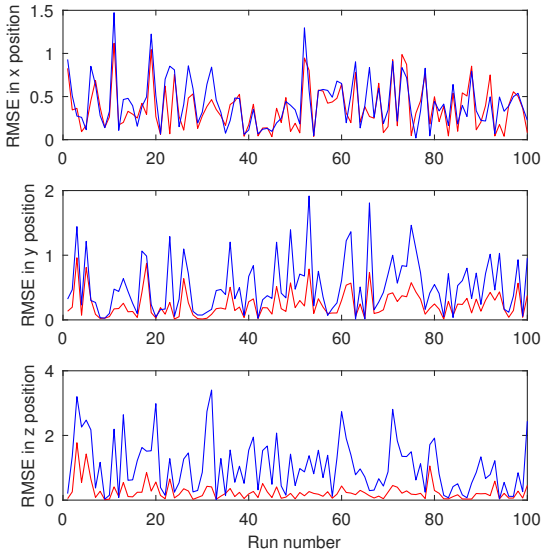

Figure 11: Rover position RMSE for the landing scenario, with (red) and without (blue) UWB

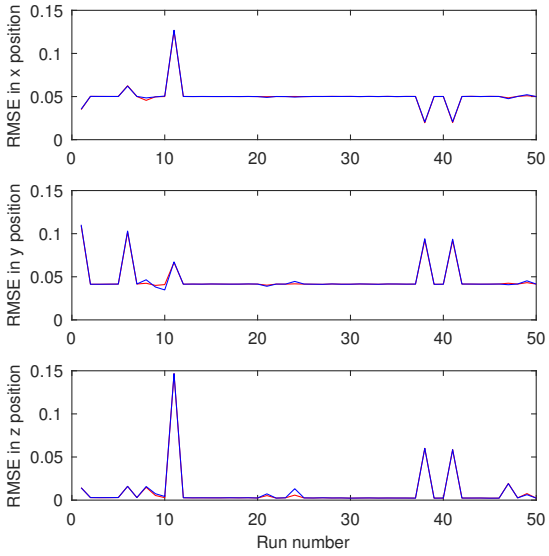

Figure 12: Rover position RMSE for the modified circle scenario, with (red) and without (blue) UWB

A similar Monte Carlo simulation is performed on a setup comparable to section V.B, but in order to compare the accuracy of the system with and without UWB, the case is assumed more ideal: the UAV is not experiencing any GNSS dropout and the UWB transponders is assumed to have infinite range. The RMSE values, averaged over all the runs, for the base station position and the attitude and position of the rover are found in Table 2. Due to the longer duration of this test, only 50 Monte Carlo simulations was run for this scenario. The UWB leads to a very slight reduction of the rover position RMSE: the norm is reduced from $7.20 \cdot 10^{-2} m$ to $7.19 \cdot 10^{-2} m$. The RMSE for each run is plotted in figure 12, where the follows the blue almost exact and is thus hardly visible. This limited reduction shows that the position accuracy in the ideal case is not affected by the inclusion of the UWB nodes, since the position accuracy for RTK GNSS is already very good.

VI. Conclusion

This paper has presented an extension to a double differenced nonlinear translational motion observer with applications for UAVs. The extension enables tight integration of ultra wideband range measurements with INS and real-time kinematic GNSS. Simulations have showed that the UWB extension increases the operational window of UAVs in GNSS-denied regions, by keeping the position error well within 1 meter, despite loss of GNSS. Also when GNSS measurements are available, but are influenced by multipath, the UWB extension showed improved performance over the GNSS-only case, particularly in the z-axis. Through a Monte Carlo simulation with 100 runs, the root mean square error for the position estimate of a UAV in landing was reduced by close to one order of magnitude when UWB measurements where included.

Acknowledgments

We thank Nadezda Sokolova for her valuable advice on GNSS, and Krzysztof Cisek for his UWB hardware expertise. This work was supported by the Norwegian Research Council (project number 223254) through the Centre for Autonomous Marine Operations and Systems at the Norwegian University of Science and Technology.

References

[1]Mahony, R., Hamel, T., and Pflimlin, J.-M., "Nonlinear complementary filters on the special orthogonal group," *IEEE Transactions on Automatic Control*, Vol. 53, No. 5, 2008, pp. 1203–1218.

[2]Mahony, R., Hamel, T., Trumpf, J., and Lageman, C., "Nonlinear Attitude Observer on SO(3) for Complementary and Compatible Measurements: A Theoretical Study," *IEEE Conference on Decision and Control*, 2009, pp. 6407–6412.

[3]Hua, M.-D., "Attitude Estimation for Accelerated Vehicles using GPS/INS Measurements," *Control Engineering Practice*, Vol. 18, 2010, pp. 723–732.

[4]Grip, H. F., Fossen, T. I., Johansen, T. A., and Saberi, A., "Attitude estimation using biased gyro and vector measurements with time-varying reference vectors," *IEEE Transactions on Automatic Control*, Vol. 57, No. 5, 2012, pp. 1332–1338.

[5]Grip, H. F., Fossen, T. I., Johansen, T. A., and Saberi, A., "Nonlinear observer for GNSS-aided inertial navigation with quaternion-based attitude estimation," *American Control Conference (ACC), 2013*, IEEE, 2013, pp. 272–279.

[6]Crassidis, J. L., Markley, F. L., and Cheng, Y., "Survey of nonlinear attitude estimation methods," *Journal of guidance, control, and dynamics*, Vol. 30, No. 1, 2007, pp. 12–28.

[7]Groves, P. D., *Principles of GNSS, Inertial, and Multisensor Integrated Navigation Systems*, Artech House, 2013.

[8]Farrell, J. A., *Aided Navigation: GPS with High Rate Sensors*, McGraw Hill, 2008.

[9]Johansen, T. A. and Fossen, T. I., "Nonlinear observer for inertial navigation aided by pseudo-range and range-rate measurements," *Control Conference (ECC), 2015 European*, IEEE, 2015, pp. 1673–1680.

[10]Hansen, J. M., Johansen, T. A., and Fossen, T. I., "Tightly Coupled Integrated Inertial and Real-Time-Kinematic Positioning Approach Using Nonlinear Observer," *American Control Conference, Boston*, 2016, pp. 1–8.

[11]Johansen, T. A. and Fossen, T. I., "Nonlinear Observer for Tightly Coupled Integration of Pseudorange and Inertial Measurements," *IEEE Transactions on Control Systems Technology*, Vol. 24, No. 6, nov 2016, pp. 2199–2206.

[12]Johansen, T. A., Hansen, J. M., and Fossen, T. I., "Nonlinear Observer for Tightly Integrated Inertial Navigation Aided by Pseudo-Range Measurements," *Journal of Dynamic Systems, Measurement, and Control*, Vol. 139, No. 1, oct 2017, pp. Paper DS–15–1088, Paper DS-15-1088.

[13]Skulstad, R., Syversen, C., Merz, M., Sokolova, N., Fossen, T., and Johansen, T., "Autonomous net recovery of fixed-wing UAV with single-frequency carrier-phase differential GNSS," *Aerospace and Electronic Systems Magazine, IEEE*, Vol. 30, No. 5, 2015, pp. 18–27.

[14]Petovello, M. G., O'Keefe, K., Chan, B., Spiller, S., Pedrosa, C., Xie, P., and Basnayake, C., "Demonstration of inter-vehicle UWB ranging to augment DGPS for improved relative positioning," *Journal of Global Positioning Systems*, Vol. 11, No. 1, 2012, pp. 11–21.

[15]Olsson, F., Rantakokko, J., and Nygards, J., "Cooperative localization using a foot-mounted inertial navigation system and ultrawideband ranging," *Indoor Positioning and Indoor Navigation (IPIN), 2014 International Conference on*, IEEE, 2014, pp. 122–131.

[16]Gross, J. N., Gu, Y., and Dewberry, B., "Tightly-Coupled GPS/UWB-Ranging for Relative Navigation During Formation Flight," *ION GNSS*, 2014.

[17]Ledergerber, A., Hamer, M., and D'Andrea, R., "A robot self-localization system using one-way ultra-wideband communication," *Intelligent Robots and Systems (IROS), 2015 IEEE/RSJ International Conference on*, Sept 2015, pp. 3131–3137.

[18]Tiemann, J., Schweikowski, F., and Wietfeld, C., "Design of an UWB indoor-positioning system for UAV navigation in GNSS-denied environments," *Indoor Positioning and Indoor Navigation (IPIN), 2015 International Conference on*, Oct 2015, pp. 1–7.

[19]Petovello, M., Feng, S., and Ochieng, W., "How do you trust centimeter level accuracy positioning?" *Inside GNSS Magazine*, Sept. 2014.

[20]MacGougan, G., O'Keefe, K., and Klukas, R., "Tightly-coupled GPS/UWB integration," *Journal of Navigation*, Vol. 63, No. 01, 2010, pp. 1–22.

[21]Monica, S. and Ferrari, G., "An experimental model for UWB distance measurements and its application to localization problems," *2014 IEEE International Conference on Ultra-WideBand (ICUWB)*, Sept 2014, pp. 297–302.

[22]Conti, A., Guerra, M., Dardari, D., Decarli, N., and Win, M. Z., "Network Experimentation for Cooperative Localization," *IEEE Journal on Selected Areas in Communications*, Vol. 30, No. 2, February 2012, pp. 467–475.

[23]Johansen, T. A., Fossen, T. I., and Goodwin, G. C., "Three-stage filter for position estimation using pseudo-range measurements," *IEEE Trans. Aerospace and Electronic Systems*, Vol. 52, 2016.

[24]Beard, R. W. and McLain, T. W., *Small Unmanned Aircraft*, Princeton University Press, 2012.

[25]Fossen, T. I., *Handbook of Marine Craft Hydrodynamics and Motion Control*, John Wiley & Sons, 2011.